Pairing a global optimization algorithm with EXAFS to accelerate prediction of lanthanide structures in solution

Thomas J. Summers,[1] Difan Zhang,[2] Josiane A. Sobrinho,[3] Ana de Bettencourt-Dias,[3] Vassiliki-Alexandra Glezakou,[4,*] and David C. Cantu[1,*]

[1] *Department of Chemical and Materials Engineering, University of Nevada, Reno, Reno, NV 89557, USA*
[2] *Physical Sciences Division, Pacific Northwest National Laboratory, Richland, WA 99352, USA*
[3] *Department of Chemistry, University of Nevada, Reno, Reno NV 89557, USA*
[4] *Oak Ridge National Laboratory, Oak Ridge, TN 37830, USA*

*Corresponding authors: glezakouva@ornl.gov, dcantu@unr.edu

ABSTRACT

Structures sampled from *ab initio* molecular dynamics (AIMD) simulations can be used to predict theoretical extended X-ray absorption fine structure (EXAFS) signals that closely match experimental spectra. However, AIMD simulations are time-consuming and resource-intensive, particularly for solvated lanthanide ions, which often form multiple non-rigid geometries with high coordination numbers. To accelerate the characterization of lanthanide structures in solution, we employed the Northwest Potential Energy Surface Search Engine (NWPEsSe), an adaptive-learning global optimization algorithm, to efficiently screen first-shell structures. As case studies, we examine two systems: $Eu(NO_3)_3$ dissolved in acetonitrile with a terpyridine ligand ($terpyNO_2$), and $Nd(NO_3)_3$ dissolved in acetonitrile. The theoretical spectra for structures identified by NWPEsSe were compared to both experimental and AIMD-derived EXAFS spectra. The NWPEsSe algorithm successfully identified the proper solvation structure for both $Eu(NO_3)_3(terpyNO_2)$ and $Nd(NO_3)(acetonitrile)_3$, with the calculated EXAFS signals closely matching the experimental spectra for the Eu-ligand complex and showing good similarity for the Nd salt; the better agreement with the ligand-containing structure is a result of a less dynamic coordination environment due to the rigid ligand. The key advantage of the global optimization algorithm lies in its ability to accelerate the structure identification process, reducing the time required from a month to a week.

INTRODUCTION

The lanthanide elements function as crucial components for a wide range of technologies, including the magnets of wind turbines, LED lights, electric vehicle batteries, and catalytic agents.[1–6] When dissolved in solution, it is uniquely challenging to characterize the structures of the lanthanide ions, as they primarily form coordination bonds through electrostatic effects rather than orbital overlaps and covalent bonding. These features lead to lanthanide ions often having large coordination numbers whose complexes can assemble in multiple low-energy, non-rigid geometries.[7] For several decades, a variety of experimental techniques[8–10] have been developed to help elucidate what these ion structures are within solution, including X-ray absorption spectroscopy (XAS). XAS, and more specifically extended X-ray absorption fine structure (EXAFS) spectroscopy, can provide insight into the local environment surrounding an ion by providing information on bond lengths, coordination numbers, and the elemental identities of first shell molecules.[11–17]

Similarly, computational techniques such as quantum mechanics (QM) calculations and molecular dynamics (MD) simulations have become invaluable tools for predicting and refining the structures of solvated ions.[18] However, these methods have their own inherent limitations for identifying molecular conformations representative of the experimental solvation structure. The initial configuration in QM structure optimizations can affect the final structure as optimization algorithms can converge structures to local minima rather than the global minimum. MD simulations might be able to compensate for this by rearranging their structures towards lower-energy configurations over the course of the simulation, but they are still restricted by the finite timescales they can cover and may fail to escape metastable states to sample alternative low-energy configurations.[19]

To overcome these limitations, high-throughput conformer sampling[20,21] and global optimization techniques have emerged as powerful methods for exploring the chemical space of systems. Such techniques like genetic algorithms,[22–26] Monte Carlo minimizations,[27–29] basin hopping,[30,31] and particle swarm optimizations[32–34] permit a systematic and accelerated search for stable structures. Among the various global optimization algorithms, the Northwest Potential Energy Search Engine (NWPEsSe)[35] stands out for its application of the bee colony algorithm[36–38] to search for global minima in complex chemical spaces. Based on the foraging behavior of

honey bee colonies, the NWPEsSe algorithm explores the chemical space using three kinds of structure construction operations ("bees"): scout bees, which search the entire chemical space randomly to discover new regions with potentially low energy configurations; employed bees, which do a local exploration of nearby unexplored regions; and onlooker bees, which explore around the low-energy structures found by the employed bees to refine the optimal solution (Figure 1). By leveraging the collective searching of these three bees, the algorithm efficiently allows convergence towards the global minimum structure without becoming trapped in local minimum basins, ensuring a comprehensive search of the chemical space.

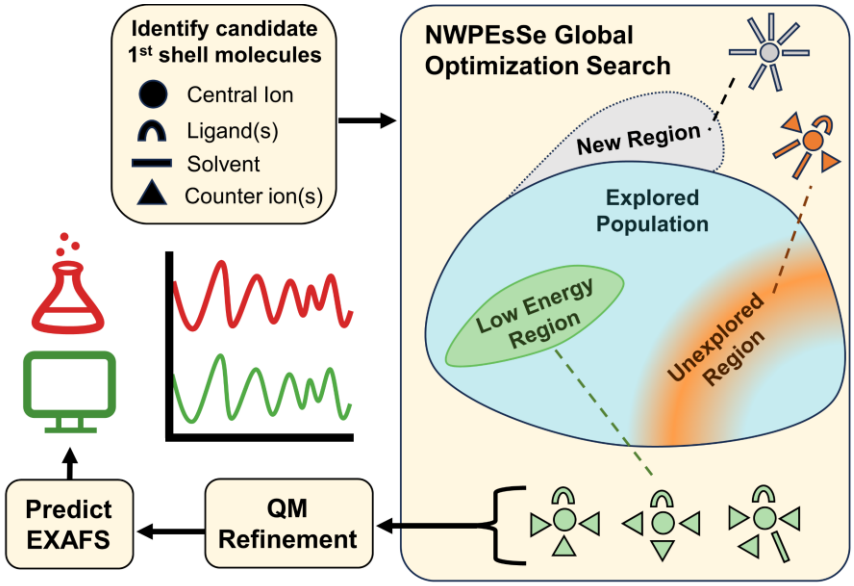

Figure 1. General schematic for using a global optimization search to screen candidate 1st shell coordination structures. Users provide information of molecules likely to be within the 1st coordination shell and NWPEsSe uses an adaptive-learning algorithm to screen potential structures. The lowest-energy structures are further refined at a QM level of theory, and the EXAFS spectra for these complexes can be compared to experimental EXAFS spectra.

Previous works have demonstrated the application of the NWPEsSe algorithm towards constructing metal and metal oxide clusters,[39–41] microsolvated amino acids,[42] and ionic liquid complexes.[43,44] In this study, we seek to expand the applicability of the NWPEsSe algorithm towards finding stable solution structures of lanthanide ion complexes, allowing the automated prediction and identification of these challenging systems. Two systems are presented in this work as case studies: $Eu(terpyNO_2)(NO_3)_3$ solvated in acetonitrile, which we previously explored using *ab initio* molecular dynamics (AIMD) simulations,[45] and $Nd(NO_3)_3$ salt solvated in

acetonitrile. To verify the accuracy of the predicted solvation structures, we compare the theoretical EXAFS spectra for the structures identified via global optimization against our previous MD-derived EXAFS spectrum (for the $Eu(terpyNO_2)(NO_3)_3$ system) and experimental EXAFS spectra. Through this approach, we seek to demonstrate the efficacy of NWPEsSe for discovering stable, experimentally verifiable lanthanide-ligand solution structures.

METHODS

Global Optimization Structure Search

The NWPEsSe global optimization algorithm[35] was used to explore the coordination configuration space of $Eu(terpyNO_2)(NO_3)_3$ (Figure 2) and $Nd(NO_3)_3$ solvated within acetonitrile. To reduce the complexity of the exploration space and direct the focus to the immediate ion coordination environment, we limited the search to only molecules that would likely be within the first coordination sphere instead of an entire solvent bath. For the solvated $Nd(NO_3)_3$, NWPEsSe constructed models where 3 NO_3^- and 4 acetonitrile molecules were positioned within a 6 Å radius sphere of a central Nd^{3+} ion. For the solvated $Eu(terpyNO_2)$ model, as we were interested in the ligated complex, NWPEsSe constructed models where the $terpyNO_2$ was first positioned at a distance 3.25 Å from the Eu^{3+} ion with the terpyridine rings oriented to coordinate the ion, followed by addition of 3 NO_3^- and 3 acetonitrile molecules within a 6 Å radius sphere of the Eu^{3+} ion. For both $Nd(NO_3)_3$ and $Eu(terpyNO_2)$ models, no additional information regarding positioning or orientation was provided for the NO_3^- and acetonitrile molecules.

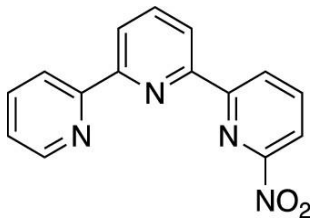

Figure 2. Structure of $terpyNO_2$ (6-nitro-2,2';6',2''-terpyridine).

To rapidly screen the stability of each structure, the NWPEsSe algorithm performed a geometry optimization using classical force fields. Each complex was centered within a large cube (edge length 21.7 Å), and the structure was relaxed using the OPLS-AA force field[46] using

previously published parameters for all of the molecules.[47–49] Non-bonded interactions were ignored beyond the 10 Å cutoff and long-range electrostatic interactions were modeled using a particle-mesh Ewald scheme.[50] The geometry optimization was carried out using GROMACS v2021.3 software.[51] The final structure and energy for each complex were fed back into the NWPEsSe algorithm to help map the chemical coordination space and guide subsequent structure designs. This process was iterated until a total of 5,000 structures were sampled; given the rather limited configuration space for the complexes, sampling this number of structures is admittedly excessive, but this ensured a robust search of the chemical space for negligible computational cost. The input example of NWPEsSe calculation is appended to the end of SI.

QM Computations

With the force-field-optimized structures obtained, we sought to further refine the first-shell geometries of the most stable complexes at a QM level of theory. Many of the candidates had optimized to near-identical coordination structures since ~1/3 of the structures designed by NWPEsSe will be refined around the identified low-energy region (Figure 1). As such, our dataset for stable, unique structures was constructed by removing all second-shell molecules from the 2,000 lowest energy structures and then removing duplicate structures with an RMSD of first-shell atoms <1 Å. The remaining unique structures (~30-50 structures) were then relaxed at a QM level of theory to improve the predicted configuration geometries and energies. Molecular geometries were optimized with the M06 functional[52] using the Stuttgard RSC Segmented basis set and corresponding effective core potentials for the Eu^{3+} and Nd^{3+} ions[53,54] and the cc-pVTZ basis set[55] for all other atoms. The complexes were modeled within an implicit solvation environment (conductor-like polarizable continuum model) of acetonitrile to mimic the bulk solvent environment.[56] After optimization, all-electron single-point energy calculations were calculated using the same procedure in our previous work.[57] The single-point energy calculations used the M06 functional, a relativistic second-order Douglas-Kroll-Hess (DKH2) Hamiltonian,[58,59] segmented all-electron relativistically contracted (SARC) basis set for the lanthanide atoms,[60] and the minimally augmented ma-def2-TZVPP basis set for the other atoms.[61] This approach allows the inclusion of the relativistic effects, which are required for accurate characterizations of lanthanide complexes.[62] All QM computations were carried out by

ORCA v5.0.2 software.[63] The DFT-optimized complex structures and corresponding energies are provided in the SI.

Molecular Dynamics Simulations

Molecular dynamics simulations were constructed of the $Nd(NO_3)_3$ system dissolved within acetonitrile following the same procedure as previously reported for the $Eu(terpyNO_2)(NO_3)_3$ system.[45] To summarize, a classical MD simulation was first conducted to equilibrate the system. The classical MD simulation was modeled with the same OPLS-AA force field and parameters used during the NWPEsSe global optimization search. The $Nd(NO_3)_3$ was dissolved within a cubic box with periodic boundary conditions containing 83 acetonitrile molecules. The system was first minimized, followed by 1 ns of NPT simulation to equilibrate the box dimension size using a 1 fs timestep. Temperature and pressure were maintained at 298 K and 1 bar using the Berendsen thermostat and barostats, respectively.[64] Long-range electrostatics were treated using a particle-mesh Ewald scheme. Nonbonded interactions were cut off at 9 Å to accommodate the smaller model volume.

After the system was equilibrated (equilibrated box edge length: 19.64 Å), an *ab initio* MD (AIMD) simulation was conducted to more accurately characterize the dynamic binding of the complex. AIMD computations were performed using the Perdew-Burke-Ernzerhof (PBE) functional[65] as implemented in the CP2K v5.1 program.[66,67] Core electrons were described by Goedecker-Teter-Hutter (GTH) pseudopotentials,[68] and valence electrons were described by a double-ζ valence polarized (DZVP) basis set;[69] the Ln^{3+} ions were described using our LnPP1 pseudopotentials and basis sets.[70] Long-range electrostatics were captured using an auxiliary plane-wave basis set with an 800 Ry cutoff. van der Waals interactions were accounted for using Grimme's D3 corrections with a 6 Å radius cutoff.[71] The simulations were conducted in the NVT ensemble at 298 K with the temperature maintained using the Nosé-Hoover thermostat.[72,73] The systems were simulated at a timestep of 1 fs until at least 10 ps of the system with a stable potential energy and consistent Nd coordination structure was obtained.

Theoretical EXAFS Spectra

EXAFS spectra for the solvated $Eu(terpyNO_2)(NO_3)_3$ and $Nd(NO_3)_3$ complexes were predicted from either the QM-optimized geometries identified by NWPEsSe or from 200

equispaced frames of the final 10 ps of the equilibrated AIMD simulation for $Nd(NO_3)_3$.[74,75] For each structure, the coordinates of the C, N, and O atoms within 6 Å of the lanthanide ion were extracted and the $\chi(k)$ spectra was computed using FEFF8.5 software.[76–78] The default Hedin-Lundqvist exchange-correlation potential and a 6 Å cutoff for the self-consistent field calculation were used. Multiple-scattering paths with up to 8 legs were included. The amplitude reduction factor (S_0^2) was set to a constant of 1.0 and no corrections were made to the Hedin-Lundqvist edge shift (ΔE_0) to align the energy grids between experiment and theory $\chi(k)$ spectra. For the NWPEsSe structures, as the theoretical EXAFS spectra are computed from single QM-optimized structures, which lack the static and thermal disorder in the shell of atoms surrounding the absorber atom that occur *in situ* (or in MD simulations), a correction of 0.005 Å was included to the mean-square displacement in half-path lengths (σ^2) to account for this disorder. This correction was not included for the $Nd(NO_3)_3$ structures sampled from the AIMD simulation. EXAFS spectra illustrating the change in predicted EXAFS upon including this correction are provided in the Supporting Information (SI).

Experimental Synthesis and EXAFS Spectra of $Nd(NO_3)_3$

To measure the spectrum of $Nd(NO_3)_3$ dissolved in acetonitrile, $Nd(NO_3)_3$ salts were purchased as hydrates from VWR and dried for 24 hours under reduced pressure and heating to 60 °C in an oven. ACS-grade acetonitrile was purchased from VWR and dried by standard methods. The salt was added to acetonitrile to obtain 0.1 M Nd^{3+} dissolved salt solution. The concentration of the solution was obtained by titrating with EDTA in the presence of xylenol orange as an indicator.[79]

EXAFS measurements at the Nd L_3-edge (6208 eV) were conducted at the Advanced Photon Source at Argonne National Laboratory (20-BM). The Si(111) monochromator was calibrated to the Fe K-edge (7112 eV). The toroidal mirror and slits provided a small X-ray beam of less than 0.7 x 0.7 mm on the samples. Higher harmonic X-rays were minimized using a Rh mirror. Transmission and fluorescence mode measurements were made with ionization chambers and a multi-element Ge solid-state detector, respectively. The $Nd(NO_3)_3$ salt was dissolved in acetonitrile immediately prior to EXAFS measurements in transmission mode. Duplicate solutions were deposited in 1 mm glass capillaries. No crystallinity or precipitate was observed in the measured solutions. Four measurements of each duplicate sample were collected and

compared, revealing no significant differences among measurements. The experimental EXAFS spectra reported are an average of all eight scans (four from each duplicate). Energy calibration was checked by simultaneously measuring a Fe K-edge (7112 eV) with a reference ionization chamber.

Analyses of the EXAFS spectra were performed using Athena from the Demeter v0.9.26 software package.[80] The experimental $\chi(k)$ spectrum was extracted from the measured spectrum using a background function with a Fourier filter cutoff distance, R_{bkg}, of 1.2 Å. In generating the Fourier transforms, the $\chi(k)$ spectra were weighted with k^2 and windowed using a Hanning function between $2.3 < k < 10.0$ Å^{-1}. The experimental and theoretical EXAFS spectra were directly compared without further fitting.

RESULTS AND DISCUSSION

Solvated Eu(terpyNO$_2$)(NO$_3$)$_3$

We begin by considering $Eu(NO_3)_3$ salt dissolved in acetonitrile in the presence of the terpyNO_2 ligand to form the complex Eu(terpyNO_2)$(NO_3)_3$, a structure we have previously characterized in both solid and solution states.[45,81] Single-crystal X-ray diffraction of this[81] and analogous complexes[82,83] revealed that in the solid state, the Eu complex has a coordination number of 10. This includes coordinate bonds to three pyridine ring nitrogen atoms and one $-NO_2$ oxygen atom of the terpyNO_2 ligand, along with 3 bidentate nitrates, resulting in a bicapped square antiprismatic geometry.

Recently, we determined the structure of this complex solvated within acetonitrile by combining experimental EXAFS data with a theoretical EXAFS spectrum obtained AIMD simulation; the solvated structure was found to be largely similar to the solid-state structure.[45] However, the AIMD simulations were computationally expensive, requiring around 600 node-hours (4 nodes each with 32 CPU-core nodes), which is not ideal for exploratory investigations where the coordination structure is unpredictable and many possible structures need to be evaluated. Likewise, the final AIMD simulation captured only ~10 ps of equilibrated simulation time. While this is sufficient for deriving theoretical EXAFS spectra, it is insufficient for sampling any alternative, thermally stable configurations. As such, we evaluate here the ability of the NWPEsSe algorithm to identify chemically reasonable coordination structures of Eu(terpyNO_2).

Following the general workflow outlined in Figure 1, the NWPEsSe algorithm was used to iteratively design 5,000 candidate structures exploring a system composed of a central Eu^{3+} ion, a terpyNO_2 ligand within the first coordination sphere, and the remaining three nitrate and three acetonitrile (ACN) molecules within either first or second coordination spheres. Of the 2,000 lowest energy structures identified at the force field level of theory (Figure S1), 69% of the structures possessed a first coordination shell composed of either Eu(terpyNO_2)$(NO_3)_3$ (21%) or Eu(terpyNO_2)$(NO_3)_3$(ACN) (48%) in various configurations.

In our previous work, we compared the theoretical EXAFS spectra of both solvent-coordinated and solvent-absent complexes, verifying the solvent-absent complex as the appropriate structure in solution.[45] The preference for the solvent-coordinated structure here is not surprising, however, for two reasons. First, the Eu^{3+} OPLS-AA parameters used in this screening were tuned to replicate the aqueous Eu^{3+} ion, and not Eu^{3+} in non-aqueous solvents, which bias the ion to higher coordination numbers—a known issue.[49] Second, since no implicit solvation model was included during force field minimization, the modeling environment may also bias the system to favor additional solvent coordination in lieu of remaining in a gas-phase second shell. One or both of these issues could be addressed by using a different approach for structure minimization, such as semiempirical PM7[84] or GFN2-xTB methods.[85] Nonetheless, the goal of this case study is to test the ability of the NWPEsSe algorithm to rapidly screen chemically-sensible Eu(terpyNO_2) complexes, and the process identified correct Eu(terpyNO_2)$(NO_3)_3$ configurations, along with reasonable Eu(terpyNO_2)$(NO_3)_3$(ACN) structures, in reduced computational time (1.75 CPU-hours for NWPEsSe screening).

Focusing on the Eu(terpyNO_2)$(NO_3)_3$ complex, the NWPEsSe search identified a total of 50 structurally unique (RMSD > 1 Å) first-shell configurations. To refine the geometries and better differentiate energetically stable configurations, the second-shell acetonitrile molecules were removed and single-point energy calculations were performed on all 50 first-shell structures at the DFT level of theory (with acetonitrile implicit solvent). The complexes within 10 kcal/mol of the lowest energy structure (23 structures in total) were then DFT-optimized, resulting in 13 structurally and energetically unique configurations (Figure S2). The lowest-energy configuration matched the one identified in our *ab initio* MD (AIMD) simulations (Figure 3). The other optimized configurations featured have unique arrangements of their nitrates and

positioning of the ion within the terpyNO_2 plane (Figure 3), but all were within 4 kcal/mol of each other and are expected to be readily accessible at room temperature.

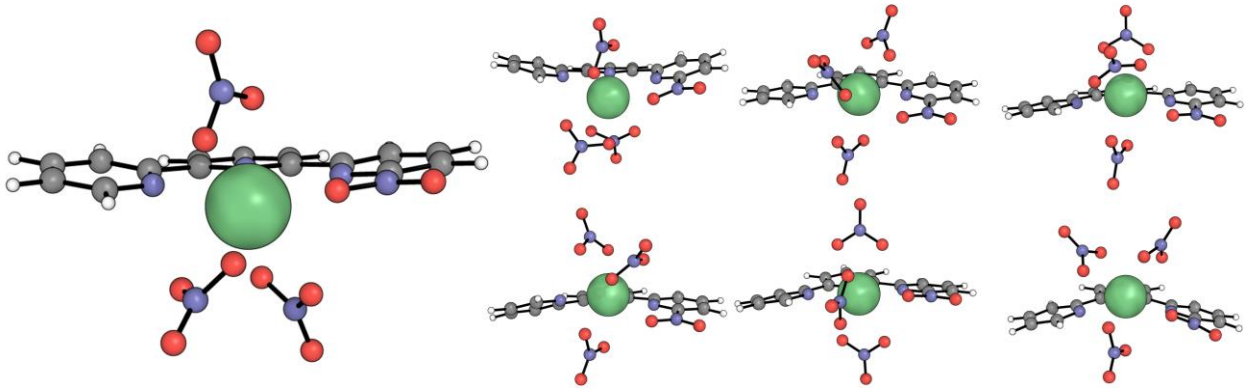

Figure 3. Ball-and-stick model of the lowest energy (left) configuration of Eu(terpyNO_2)$(NO_3)_3$ and six other examples of low-energy configurations identified by the NWPEsSe algorithm. Color scheme: Eu (green), C (gray), H (white), O (red), N (blue).

Theoretical EXAFS spectra were computed for the 13 DFT-optimized configurations and averaged to produce a single theoretical EXAFS spectrum representing the NWPEsSe-sampled structures. The $\chi(k)$ signal and k^2-weighted Fourier transform spectrum of this theoretical spectrum are overlaid against the experimental signal, along with the results from our previous AIMD simulation (Figure 4; theoretical spectrum without the σ^2 approximation included provided in Figure S3). While the AIMD and NWPEsSe-derived theoretical spectra both show remarkable agreement with the experimental data in the frequency and shape of the $\chi(k)$ oscillations, the NWPEsSe-derived spectrum shows a distinct improvement in matching the experimental data. The origin of this improvement is evident in the Fourier-transformed signal, which indicates that the Eu-atom distances and spatial positioning in the NWPEsSe sampled configurations mirror the experimental structures and lead to the close alignment in their signals. In contrast, the AIMD-derived signal shows a slight shift to the right of the experimental peaks, indicating slightly longer Eu-atom distances in the simulation compared to those distances in the experiment.

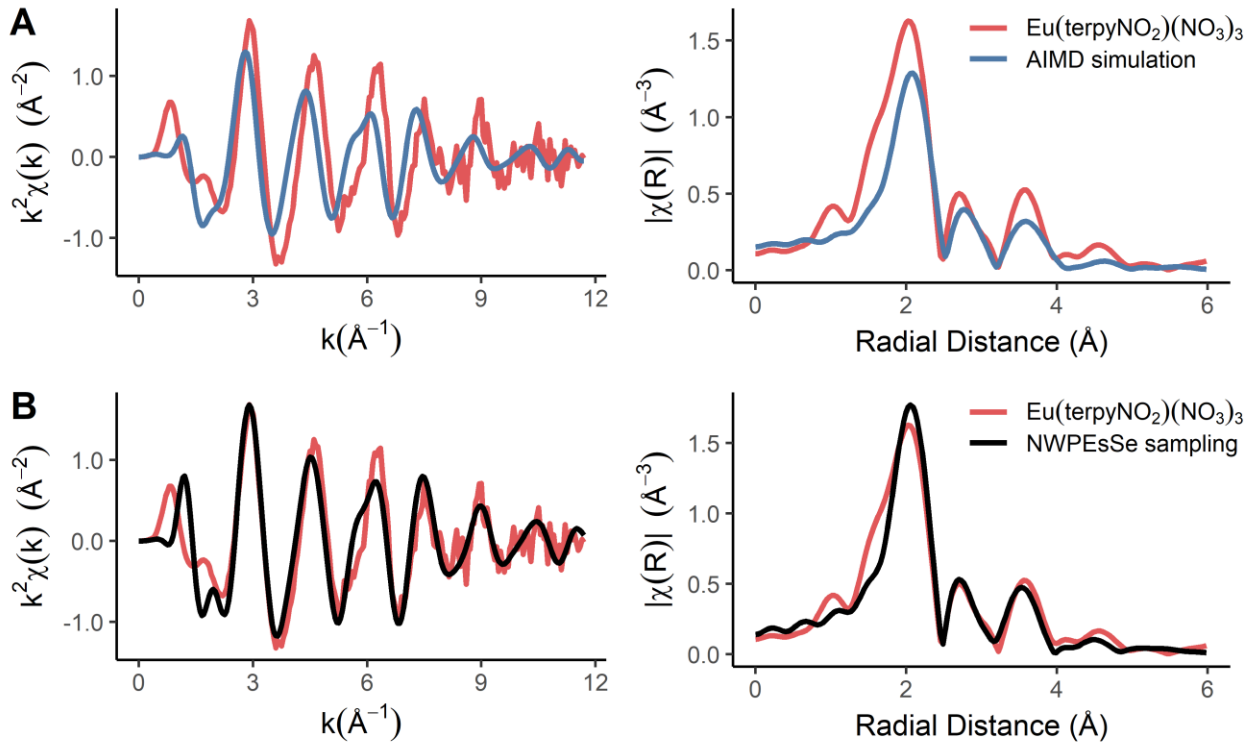

Figure 4. Overlay of the experimental EXAFS spectrum (red) for the Eu L_3-edge of $Eu(terpyNO_2)(NO_3)_3$ dissolved in acetonitrile compared to theoretical spectra predicted from (A) AIMD simulation and (B) NWPEsSe sampled structures.

While the moderate improvement in the calculated EXAFS signal is notable, the most significant advancements from this alternative workflow are twofold: (1) the workflow not only successfully identified the correct core structure but also generated a diverse array of low-lying alternative configurations that were absent in the AIMD simulation; and (2) the results were obtained with significantly accelerated speed—approximately 275 node hours (1 node with 32 CPU-core nodes) with QM-computations of individual structures able to be run in parallel to reduce real-world time compared to the AIMD simulation.

Solvated $Nd(NO_3)_3$

To investigate a system where the Ln^{3+} ion is not exclusively chelated by rigid, multidentate ligands, we modeled the structure of $Nd(NO_3)_3$ dissolved in acetonitrile. Following the same protocol reported previously for the $Eu(terpyNO_2)(NO_3)_3$ system,[45] an AIMD simulation was designed and run for $Nd(NO_3)_3$. The resulting Ln-anion-solvent complex formed during the initial force field equilibration was $Nd(NO_3)_3(ACN)_4$ with a coordination number of

10. This is larger than the coordination number of the aqua complex $[Nd(H_2O)_9]^{3+}$,[12] but no coordinated acetonitrile molecules dissociated from the Nd during AIMD equilibration or production-level simulations, indicating the structure remained stable for at least 11 ps. Structures from the final 10 ps of the equilibrated AIMD simulation were used to construct a theoretical EXAFS signal.

The NWPEsSe algorithm was similarly employed to iteratively design first shell structures exploring different configurations of a system containing $Nd(NO_3)_3(ACN)_4$. Interestingly, of the 2,000 lowest-energy structures (Figure S4), nearly all favored the 9-coordinate $Nd(NO_3)_3(ACN)_3$ (95%) over the 10-coordinate complex. To investigate further the difference between the two complex configurations, we analyzed the coordination structures identified by the NWPEsSe algorithm for both first-shell configurations. After removing duplicates, the unique configurations of $Nd(NO_3)_3(ACN)_3$ and $Nd(NO_3)(ACN)_4$ were DFT-optimized, resulting in 7 unique first-shell structures of $Nd(NO_3)_3(ACN)_3$ (Figure S5) and 10 of $Nd(NO_3)_3(ACN)_4$ (Figure S6). Despite the diversity of the configurations identified, all structures were computed to be within 4 kcal/mol of their respective lowest energy configurations (Figure 5).

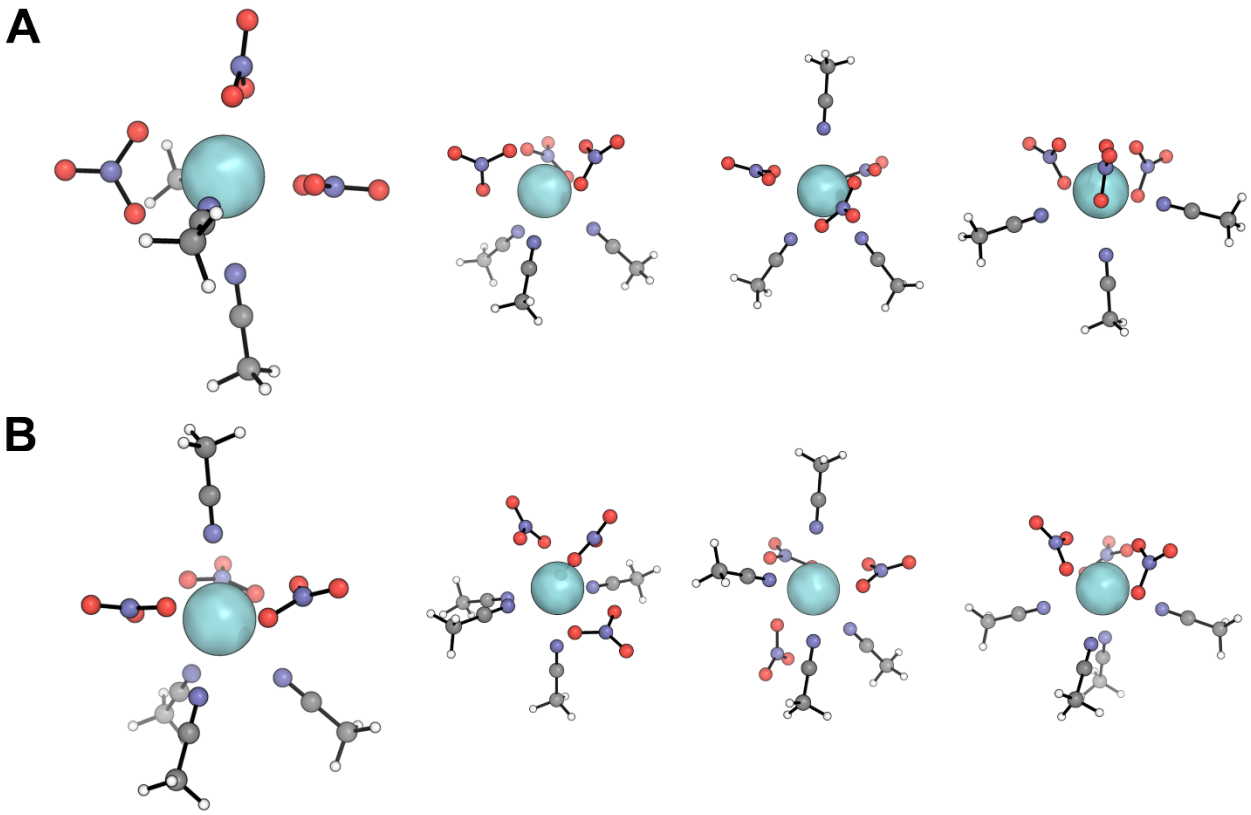

Figure 5. Ball-and-stick models of the lowest energy configuration (*left*) of (A) $Nd(NO_3)_3(ACN)_3$ and (B) $Nd(NO_3)(ACN)_4$ along with examples of other stable configurations (*right*) identified by NWPEsSe. Color scheme: Nd (cyan), C (gray), H (white), O (red), N (blue).

Theoretical EXAFS spectra were computed for each of the DFT-optimized configurations and averaged to produce a single theoretical EXAFS spectrum for both complexes. The $\chi(k)$ signal and k^2-weighted Fourier transform spectra were each overlaid with the experimental signal in Figure 6, alongside results from the AIMD simulation of $Nd(NO_3)_3(ACN)_4$.

Comparing the $\chi(k)$ signal from the AIMD-derived results to the experimental data (Figure 6A), there is a great similarity between the two spectra in terms of peak positioning and shape, with only a slight offset in the AIMD spectrum. The Fourier-transformed spectrum also shows similarity, with the peaks and shouldering at ~2.0, 2.6, 3.6, and 4.1 Å being reproduced, though slightly offset from the experimental data. Direct comparison of the AIMD-derived spectrum to that from the NWPEsSe-identified structures highlights the differences caused by explicitly modeling changes in Nd-atom bond lengths in the simulation versus using a constant σ^2 in the EXAFS calculation to mimic the dynamics. The results (Figure S7) show that while the positions of the $\chi(k)$ peaks and troughs are nearly identical, the shape and amplitude begin to diverge as k increases. The Fourier-transformed spectra show similar peaks from single

scattering of the coordinating N and O atoms (~2.0 and 2.6 Å); however, despite having the same spectral shape in the later region of the FT-spectrum (e.g. the broadened peak at ~4.5 Å), these peaks that arise from forward scattering of acetonitrile N-C and nitrate N-O (~3.5 Å) and other multi-scattering paths are right-shifted. The right-shifting of the peaks is also shown to not originate from the inclusion of the σ^2 constant (Figure S8). These differences suggest that the different dynamics between Nd-O(nitrate) and Nd-N(acetonitrile) coordination bonds require explicit modeling beyond a σ^2 term approximation for accurate replication. Nevertheless, since the shape of the spectra remains consistent and only shifted, the results from the NWPEsSe-sampled structures can provide valuable insight for quicker comparison of different first-shell structures.

When comparing the theoretical spectra for the 3- and 4-acetonitrile coordinated complexes generated from NWPEsSe (black lines in Figure 6B and 6C), the two spectra are very similar, with only small differences in the shapes of their $\chi(k)$ and Fourier-transformed signals. The 3-acetonitrile complex shows slightly better agreement with the experimental spectrum, including better alignment of the principal peaks in the $\chi(k)$ and the single scattering peak ~2.0 in the Fourier-transformed spectra, indicating a more accurate replication of the coordinating atom-Nd distances. Additionally, the presence of distinct peaks in the 4 – 6 Å region of the Fourier-transformed spectrum better matches the distinct experimental peaks (though right-shifted) compared to the broadened band of the 4-solvent complex.

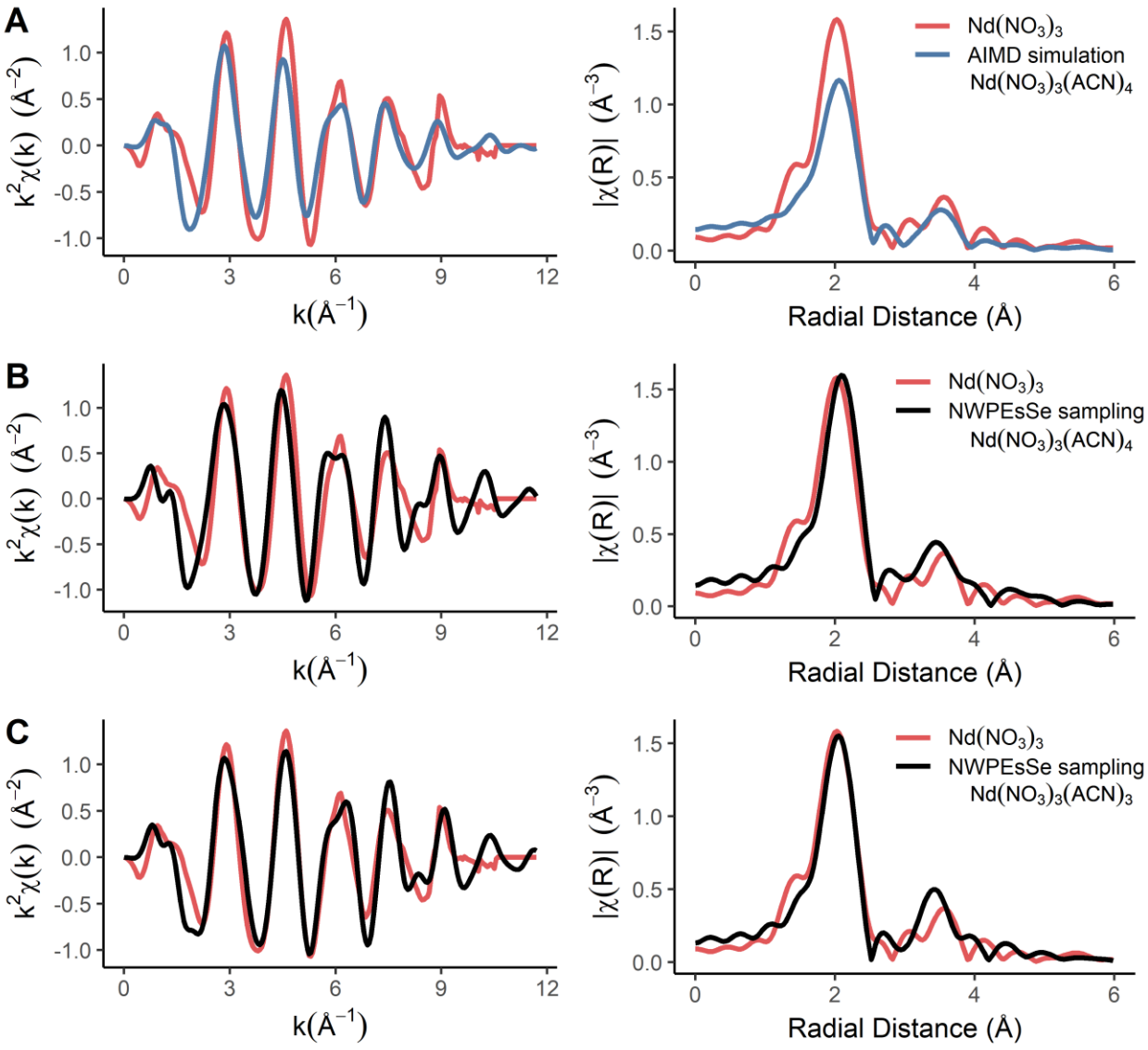

Figure 6. Overlay of EXAFS spectra for the Nd L_3-edge of $Nd(NO_3)_3$ solvated in acetonitrile comparing the experimental spectrum (red, A - C) to spectra of $Nd(NO_3)_3(ACN)_4$ predicted from (A) AIMD simulation and (B) NWPEsSe, as well as to (C) the spectrum predicted of structures of $Nd(NO_3)_3(ACN)_3$ obtained from NWPEsSe.

Since these spectral features arise from calculations on QM-optimized structures, as opposed to mathematically fitting between theory and experimental spectra, they suggest that the experimental structure is more likely $Nd(NO_3)_3(ACN)_3$ rather than $Nd(NO_3)_3(ACN)_4$, though these small differences alone are not conclusive without further evidence. Previously reported FT-IR experiments reported an average coordination number of 9.0 for $Nd(NO_3)_3$ within acetonitrile,[86] which is consistent with our findings that the NWPEsSe-sampled 9-coordinate

$Nd(NO_3)_3(ACN)_3$ structures better match the experimental EXAFS. While an additional AIMD simulation of the $Nd(NO_3)_3(ACN)_3$ complex could further support these findings, the primary goal here is to evaluate the effectiveness of the NWPEsSe algorithm towards identifying the solvation structure. Remarkably, the NWPEsSe algorithm not only identified the correct first shell structure between two similar, stable configurations but it obtained its results at a significantly faster speed: while the AIMD simulation took ~600 node hours (4 nodes with 32 CPU-core nodes) QM-optimizing all the structures derived from the NWPEsSe algorithm took ~300 node hours (32 CPU-core nodes) with the computations for individual structures run in parallel. The differences in compute times for both approaches are summarized in Table 1.

Table 1. Summary of approximate compute times for AIMD and NWPEsSe approaches.

	AIMD simulation approach		**NWPEsSe algorithm approach**		
Model System	AIMD compute time *(node hours; four 32 CPU-core nodes)*	Real-world time *(days)*	NWPEsSe search *(CPU hours)*	QM refinement *(node hours; one 32 CPU-core node per structure)*	Real-world time *(days)*
$Eu(terpyNO_2)(NO_3)_3$	600	25	1.75	275	3
$Nd(NO_3)_3$	600	25	1.5	300	3

CONCLUSIONS

Agreement between predicted and measured EXAFS spectra is a robust method to determine whether the structures used to calculate the predicted signal are representative of those in solution. Typically, these structures are sampled from MD simulation snapshots to capture the first-shell structure and time-averaged ion-ligand bond distances. Obtaining reliable MD simulation structures for lanthanide complexes is challenging because MD simulations are biased by the starting configuration. Further, more accurate AIMD simulations are resource- and time-intensive, and they only sample a limited chemical space.

We explored the use of the NWPEsSe global optimization algorithm to preliminarily screen first-shell structures for further DFT refinement. We focused on two systems for this case

study: Eu(terpyNO$_2$)(NO$_3$)$_3$ dissolved in acetonitrile and Nd(NO$_3$)$_3$ dissolved in acetonitrile. For the Eu(terpyNO$_2$)(NO$_3$)$_3$ system, the NWPEsSe algorithm successfully identified the correct Eu(terpyNO$_2$)(NO$_3$)$_3$ coordination structure along with 12 other low-energy configurations not observed in a previously reported AIMD simulation. The theoretical EXAFS spectrum calculated from the NWPEsSe-identified structures showed a near-perfect match with the experimental spectrum.

For the Nd(NO$_3$)$_3$ system, both an AIMD simulation and NWPEsSe search were conducted. The AIMD simulation indicated a stable Nd(NO$_3$)$_3$(ACN)$_4$ structure while the NWPEsSe search identified the Nd(NO$_3$)$_3$(ACN)$_3$ structure as the preferential structure. To investigate this discrepancy, both 3- and 4-solvent coordinated complexes identified by NWPEsSe were DFT-optimized, and their predicted spectra were compared to the experimental data. While the spectral differences between the two complexes were subtle, the 3-solvent complex identified by NWPEsSe showed slightly better agreement in the first-shell Nd-atom distances and spectral features. The spectra computed from the NWPEsSe structures exhibited slight amplitude differences and offsets for later regions of the $\chi(k)$ and Fourier-transformed spectra, respectively, likely due to the difference between explicitly sampling dynamic bond distances in MD simulations versus using a constant σ^2 term to approximate these changes. This difference was observed in the Nd(NO$_3$)$_3$(ACN)$_3$ system but not in the Eu(terpyNO$_2$)(NO$_3$)$_3$ system, likely due to more dynamic bonding between monodentate acetonitrile and bidentate nitrate compared to the more rigid nitrate and terpyNO$_2$ ligands. The finding that Nd(NO$_3$)$_3$(ACN)$_3$ is the predominant solution structure aligns with previous FT-IR reports.[86]

The most practical advantage of the global optimization approach is the significantly faster identification of the first shell structures. By focusing DFT computations on unique low-energy structures identified by NWPEsSe, batch computations can be run in parallel for individual structures, reducing the real-time computation from approximately one month (for AIMD simulation) to less than a week (for NWPEsSe sampling). Lanthanide systems with more dynamic first shells may benefit from additional MD modeling to improve the predicted EXAFS spectrum (as seen with the Nd(NO$_3$)$_3$ case) but an initial search with NWPEsSe to screen first shell structures can reduce the potential for performing AIMD simulations on improper structures.

As modeling methods that include *f*-block element chemistry continues to evolve and improve in both chemical accuracy and computational speed, we anticipate semi-empirical approaches (e.g. GFN2-xTB), machine-learned interatomic potentials (e.g. MACE-MP-0 or M3GNet)[87,88] or new lanthanide force fields[89] will provide more efficient screenings at a minimal increase in computational cost. Overall, this study serves as a proof-of-concept that combining global optimization algorithms like NWPEsSe with experimental EXAFS can be a viable approach for characterizing unresolved lanthanide-ligand solution structures.

SUPPORTING INFORMATION

Additional molecular figures and EXAFS spectra comparison (PDF) and coordinates of the DFT-optimized structures (TXT).

ACKNOWLEDGMENTS

The authors thank Dr. Shelly Kelly (Beamline Scientist, Advanced Photon Source at Argonne National Laboratory) for support with the EXAFS measurements. This material is based on work supported by the U.S. Department of Energy (DOE), Office of Basic Energy Sciences under Award DE-SC0022178. D.Z. acknowledges the U.S. Department of Energy (DOE), Office of Science, Office of Basic Energy Sciences, Chemical Sciences, Geosciences, and Biosciences Division FWP 81462. This research used resources of the Advanced Photon Source, a U.S. Department of Energy (DOE) Office of Science user facility operated for the DOE Office of Science by Argonne National Laboratory under Contract No. DE-AC02-06CH11357. This research used resources of the National Energy Research Scientific Computing Center (NERSC), a Department of Energy Office of Science User Facility using NERSC award BES-ERCAP0021496 and BES-ERCAP0023505.

ORCiD

Thomas J. Summers: 0000-0002-4243-6078
Difan Zhang: 0000-0001-7530-2378
Ana de Bettencourt-Dias: 0000-0001-5162-2393
Vassiliki-Alexandra Glezakou: 0000-0001-6028-7021
David C. Cantu: 0000-0001-9584-5062

REFERENCES

(1) Balaram, V. Rare Earth Elements: A Review of Applications, Occurrence, Exploration, Analysis, Recycling, and Environmental Impact. *Geosci. Front.* **2019**, *10* (4), 1285–1303. https://doi.org/10.1016/j.gsf.2018.12.005.

(2) Tsurugi, H.; Mashima, K. Renaissance of Homogeneous Cerium Catalysts with Unique Ce(IV/III) Couple: Redox-Mediated Organic Transformations Involving Homolysis of Ce(IV)–Ligand Covalent Bonds. *J. Am. Chem. Soc.* **2021**, *143* (21), 7879–7890. https://doi.org/10.1021/jacs.1c02889.

(3) *Modern Applications of Lanthanide Luminescence*; de Bettencourt-Dias, A., Ed.; Springer Series on Fluorescence; Springer International Publishing: Cham, 2023; Vol. 19. https://doi.org/10.1007/978-3-031-12859-2.

(4) Mikami, K.; Terada, M.; Matsuzawa, H. "Asymmetric" Catalysis by Lanthanide Complexes. *Angew. Chem. Int. Ed.* **2002**, *41* (19), 3554–3572. https://doi.org/10.1002/1521-3773(20021004)41:19<3554::AID-ANIE3554>3.0.CO;2-P.

(5) Bettencourt-Dias, A. de. Lanthanide-Based Emitting Materials in Light-Emitting Diodes. *Dalton Trans.* **2007**, No. 22, 2229–2241. https://doi.org/10.1039/B702341C.

(6) Qiao, Y.; Schelter, E. J. Lanthanide Photocatalysis. *Acc. Chem. Res.* **2018**, *51* (11), 2926–2936. https://doi.org/10.1021/acs.accounts.8b00336.

(7) Bünzli, J.-C. G. Benefiting from the Unique Properties of Lanthanide Ions. *Acc. Chem. Res.* **2006**, *39* (1), 53–61. https://doi.org/10.1021/ar0400894.

(8) Simon, J. D.; Moomaw, W. R.; Ceckler, T. M. The Structure and NMR and Electronic Spectra of Europium(III) Crown Ether Complexes in Solution. *J. Phys. Chem.* **1985**, *89* (26), 5659–5665. https://doi.org/10.1021/j100272a017.

(9) Latva, M.; Takalo, H.; Mukkala, V.-M.; Kankare, J. Evaluation of Solution Structures of Highly Luminescent Europium(III) Chelates by Using Laser Induced Excitation of the 7F0 → 5D0 Transition. *Inorganica Chim. Acta* **1998**, *267* (1), 63–72. https://doi.org/10.1016/S0020-1693(97)05553-9.

(10) Gateau, C.; Mazzanti, M.; Pécaut, J.; Dunand, F. A.; Helm, L. Solid-State and Solution Properties of the Lanthanide Complexes of a New Nonadentate Tripodal Ligand Derived from 1,4,7-Triazacyclononane. *Dalton Trans.* **2003**, No. 12, 2428–2433. https://doi.org/10.1039/B303079B.

(11) Yaita, T.; Narita, H.; Suzuki, Sh.; Tachimori, Sh.; Motohashi, H.; Shiwaku, H. Structural Study of Lanthanides(III) in Aqueous Nitrate and Chloride Solutions by EXAFS. *J. Radioanal. Nucl. Chem.* **1999**, *239* (2), 371–375. https://doi.org/10.1007/BF02349514.

(12) Shiery, R. C.; Fulton, J. L.; Balasubramanian, M.; Nguyen, M.-T.; Lu, J.-B.; Li, J.; Rousseau, R.; Glezakou, V.-A.; Cantu, D. C. Coordination Sphere of Lanthanide Aqua Ions Resolved with Ab Initio Molecular Dynamics and X-Ray Absorption Spectroscopy. *Inorg. Chem.* **2021**, *60* (5), 3117–3130. https://doi.org/10.1021/acs.inorgchem.0c03438.

(13) Stumpf, S.; Billard, I.; Gaillard, C.; Panak, P. J.; Dardenne, K. TRLFS and EXAFS Investigations of Lanthanide and Actinide Complexation by Triflate and Perchlorate in an Ionic Liquid. *Radiochim. Acta* **2008**, *96* (1), 1–10. https://doi.org/10.1524/ract.2008.1461.

(14) Persson, I.; D'Angelo, P.; De Panfilis, S.; Sandström, M.; Eriksson, L. Hydration of Lanthanoid(III) Ions in Aqueous Solution and Crystalline Hydrates Studied by EXAFS Spectroscopy and Crystallography: The Myth of the "Gadolinium Break." *Chem. Eur. J.* **2008**, *14* (10), 3056–3066. https://doi.org/10.1002/chem.200701281.

(15) Moreau, J.; Guillon, E.; Pierrard, J.-C.; Rimbault, J.; Port, M.; Aplincourt, M. Complexing Mechanism of the Lanthanide Cations Eu3+, Gd3+, and Tb3+ with 1,4,7,10-Tetrakis(Carboxymethyl)-1,4,7,10-Tetraazacyclododecane (Dota)—Characterization of Three Successive Complexing Phases: Study of the Thermodynamic and Structural Properties of the Complexes by Potentiometry, Luminescence Spectroscopy, and EXAFS. *Chem. Eur. J.* **2004**, *10* (20), 5218–5232. https://doi.org/10.1002/chem.200400006.
(16) Narita, H.; Yaita, T.; Suzuki, S.; Takai, K.; Tachimori, S.; Motohashi, H.; IUCr. Structural studies of lanthanide(III) complexes with oxydiacetic acid and iminodiacetic acid in aqueous solution by EXAFS. *J. Synchrotron Rad.* **2001**, 8, 672-673. https://doi.org/10.1107/S0909049500017180.
(17) Brigham, D. M.; Ivanov, A. S.; Moyer, B. A.; Delmau, L. H.; Bryantsev, V. S.; Ellis, R. J. Trefoil-Shaped Outer-Sphere Ion Clusters Mediate Lanthanide(III) Ion Transport with Diglycolamide Ligands. *J. Am. Chem. Soc.* **2017**, *139* (48), 17350–17358. https://doi.org/10.1021/jacs.7b07318.
(18) Cantu, D. C. Chapter Seven - Predicting Lanthanide Coordination Structures in Solution with Molecular Simulation. In *Methods in Enzymology*; Cotruvo, J. A., Ed.; Rare-Earth Element Biochemistry: Characterization and Applications of Lanthanide-Binding Biomolecules; Academic Press, 2021; Vol. 651, pp 193–233. https://doi.org/10.1016/bs.mie.2021.02.002.
(19) Pietrucci, F. Strategies for the Exploration of Free Energy Landscapes: Unity in Diversity and Challenges Ahead. *Rev. Phys.* **2017**, *2*, 32–45. https://doi.org/10.1016/j.revip.2017.05.001.
(20) Taylor, M. G.; Burrill, D. J.; Janssen, J.; Batista, E. R.; Perez, D.; Yang, P. Architector for High-Throughput Cross-Periodic Table 3D Complex Building. *Nat. Commun.* **2023**, *14* (1), 2786. https://doi.org/10.1038/s41467-023-38169-2.
(21) Summers, T.; Taylor, M.; Augustine, L.; Janssen, J.; Perez, D.; Batista, E.; Yang, P. On the Importance of Configuration Search to the Predictivity of Lanthanide Selectivity. *ChemRxiv*. August 19, 2024. https://doi.org/10.26434/chemrxiv-2024-2112n.
(22) Hartke, B. Global Geometry Optimization of Clusters Using Genetic Algorithms. *J. Phys. Chem.* **1993**, *97* (39), 9973–9976. https://doi.org/10.1021/j100141a013.
(23) Deaven, D. M.; Ho, K. M. Molecular Geometry Optimization with a Genetic Algorithm. *Phys. Rev. Lett.* **1995**, *75* (2), 288–291. https://doi.org/10.1103/PhysRevLett.75.288.
(24) Brain, Z. E.; Addicoat, M. A. Optimization of a Genetic Algorithm for Searching Molecular Conformer Space. *J. Chem. Phys.* **2011**, *135* (17), 174106. https://doi.org/10.1063/1.3656323.
(25) Supady, A.; Blum, V.; Baldauf, C. First-Principles Molecular Structure Search with a Genetic Algorithm. *J. Chem. Inf. Model.* **2015**, *55* (11), 2338–2348. https://doi.org/10.1021/acs.jcim.5b00243.
(26) Niesse, J. A.; Mayne, H. R. Global Optimization of Atomic and Molecular Clusters Using the Space-Fixed Modified Genetic Algorithm Method. *J. Comput. Chem.* **1997**, *18* (9), 1233–1244. https://doi.org/10.1002/(SICI)1096-987X(19970715)18:9<1233::AID-JCC11>3.0.CO;2-6.
(27) Li, Z.; Scheraga, H. A. Structure and Free Energy of Complex Thermodynamic Systems. *J. Mol. Struct. THEOCHEM* **1988**, *179* (1), 333–352. https://doi.org/10.1016/0166-1280(88)80133-7.

(28) Carnevali, P.; Tóth, G.; Toubassi, G.; Meshkat, S. N. Fast Protein Structure Prediction Using Monte Carlo Simulations with Modal Moves. *J. Am. Chem. Soc.* **2003**, *125* (47), 14244–14245. https://doi.org/10.1021/ja036647b.
(29) Roth, M.; Toker, Y.; Major, D. T. Monte Carlo-Simulated Annealing and Machine Learning-Based Funneled Approach for Finding the Global Minimum Structure of Molecular Clusters. *ACS Omega* **2024**, *9* (1), 1298–1309. https://doi.org/10.1021/acsomega.3c07600.
(30) White, R. P.; Mayne, H. R. An Investigation of Two Approaches to Basin Hopping Minimization for Atomic and Molecular Clusters. *Chem. Phys. Lett.* **1998**, *289* (5), 463–468. https://doi.org/10.1016/S0009-2614(98)00431-X.
(31) Wales, D. J.; Scheraga, H. A. Global Optimization of Clusters, Crystals, and Biomolecules. *Science* **1999**, *285* (5432), 1368–1372. https://doi.org/10.1126/science.285.5432.1368.
(32) Call, S. T.; Zubarev, D. Yu.; Boldyrev, A. I. Global Minimum Structure Searches via Particle Swarm Optimization. *J. Comput. Chem.* **2007**, *28* (7), 1177–1186. https://doi.org/10.1002/jcc.20621.
(33) Wang, Y.; Lv, J.; Zhu, L.; Ma, Y. Crystal Structure Prediction via Particle-Swarm Optimization. *Phys. Rev. B* **2010**, *82* (9), 094116. https://doi.org/10.1103/PhysRevB.82.094116.
(34) Agrawal, S.; Silakari, S. Fletcher–Reeves Based Particle Swarm Optimization for Prediction of Molecular Structure. *J. Mol. Graph. Model.* **2014**, *49*, 11–17. https://doi.org/10.1016/j.jmgm.2014.01.001.
(35) Zhang, J.; Glezakou, V.-A.; Rousseau, R.; Nguyen, M.-T. NWPEsSe: An Adaptive-Learning Global Optimization Algorithm for Nanosized Cluster Systems. *J. Chem. Theory Comput.* **2020**, *16* (6), 3947–3958. https://doi.org/10.1021/acs.jctc.9b01107.
(36) Karaboga, D.; others. An Idea Based on Honey Bee Swarm for Numerical Optimization; Technical Report TR06, **2005**, Erciyes Univ., Kayseri, Turkey.
(37) Zhang, J.; Dolg, M. ABCluster: The Artificial Bee Colony Algorithm for Cluster Global Optimization. *Phys. Chem. Chem. Phys.* **2015**, *17* (37), 24173–24181. https://doi.org/10.1039/C5CP04060D.
(38) Zhang, J.; Dolg, M. Global Optimization of Clusters of Rigid Molecules Using the Artificial Bee Colony Algorithm. *Phys. Chem. Chem. Phys.* **2016**, *18* (4), 3003–3010. https://doi.org/10.1039/C5CP06313B.
(39) Liu, B.; Yang, J. Thermochemical Properties and Growth Mechanism of the Ag-Doped Germanium Clusters, AgGenλ with n = 1–13 and λ = −1, 0, and +1. *ACS Omega* **2021**, *6* (14), 9813–9827. https://doi.org/10.1021/acsomega.1c00501.
(40) Bhowmick, S.; Maisser, A.; Suleimanov, Y. V.; Schmidt-Ott, A.; Biskos, G. Electronic Structure, Stability, and Electrical Mobility of Cationic Silver Oxide Atomic Clusters. *J. Phys. Chem. A* **2022**, *126* (37), 6376–6386. https://doi.org/10.1021/acs.jpca.2c02809.
(41) Yang, Z.; Cao, Z.; Rehman, A. U.; Yang, J. Structural Evolution, Electronic Structures, and Vibrational Properties of Anionic LuGen (n = 5–17) Clusters: From Lu-Linked to Lu-Encapsulated Configurations. *Inorg. Chem.* **2021**, *60* (18), 14446–14456. https://doi.org/10.1021/acs.inorgchem.1c02247.
(42) Johnson, S. I.; Baer, M. D.; Raugei, S. Protonation of Serine in Gas and Condensed and Microsolvated States in Aqueous Solution. *J. Phys. Chem. A* **2022**, *126* (1), 44–52. https://doi.org/10.1021/acs.jpca.1c08795.

(43) Zhang, J.; Baxter, E. T.; Nguyen, M.-T.; Prabhakaran, V.; Rousseau, R.; Johnson, G. E.; Glezakou, V.-A. Structure and Stability of the Ionic Liquid Clusters [EMIM]n[BF4]N+1– (n = 1–9): Implications for Electrochemical Separations. *J. Phys. Chem. Lett.* **2020**, *11* (16), 6844–6851. https://doi.org/10.1021/acs.jpclett.0c01671.
(44) Tan, S.; Zhang, D.; Nguyen, M.-T.; Shutthanandan, V.; Varga, T.; Rousseau, R.; Johnson, G. E.; Glezakou, V.-A.; Prabhakaran, V. Tuning the Charge and Hydrophobicity of Graphene Oxide Membranes by Functionalization with Ionic Liquids at Epoxide Sites. *ACS Appl. Mater. Interfaces* **2022**, *14* (16), 19031–19042. https://doi.org/10.1021/acsami.2c02366.
(45) Summers, T. J.; Sobrinho, J. A.; de Bettencourt-Dias, A.; Kelly, S. D.; Fulton, J. L.; Cantu, D. C. Solution Structures of Europium Terpyridyl Complexes with Nitrate and Triflate Counterions in Acetonitrile. *Inorg. Chem.* **2023**, *62* (13), 5207–5218. https://doi.org/10.1021/acs.inorgchem.3c00199.
(46) Jorgensen, W. L.; Maxwell, D. S.; Tirado-Rives, J. Development and Testing of the OPLS All-Atom Force Field on Conformational Energetics and Properties of Organic Liquids. *J. Am. Chem. Soc.* **1996**, *118* (45), 11225–11236. https://doi.org/10.1021/ja9621760.
(47) Pothoczki, S.; Pusztai, L. Intermolecular Orientations in Liquid Acetonitrile: New Insights Based on Diffraction Measurements and All-Atom Simulations. *J. Mol. Liq.* **2017**, *225*, 160–166. https://doi.org/10.1016/j.molliq.2016.11.056.
(48) Doherty, B.; Zhong, X.; Gathiaka, S.; Li, B.; Acevedo, O. Revisiting OPLS Force Field Parameters for Ionic Liquid Simulations. *J. Chem. Theory Comput.* **2017**, *13* (12), 6131–6145. https://doi.org/10.1021/acs.jctc.7b00520.
(49) Baaden, M.; Berny, F.; Madic, C.; Wipff, G. M3+ Lanthanide Cation Solvation by Acetonitrile: The Role of Cation Size, Counterions, and Polarization Effects Investigated by Molecular Dynamics and Quantum Mechanical Simulations. *J. Phys. Chem. A* **2000**, *104* (32), 7659–7671. https://doi.org/10.1021/jp001352v.
(50) Essmann, U.; Perera, L.; Berkowitz, M. L.; Darden, T.; Lee, H.; Pedersen, L. G. A Smooth Particle Mesh Ewald Method. *J. Chem. Phys.* **1995**, *103* (19), 8577–8593. https://doi.org/10.1063/1.470117.
(51) Abraham, M. J.; Murtola, T.; Schulz, R.; Páll, S.; Smith, J. C.; Hess, B.; Lindahl, E. GROMACS: High Performance Molecular Simulations through Multi-Level Parallelism from Laptops to Supercomputers. *SoftwareX* **2015**, *1–2*, 19–25. https://doi.org/10.1016/j.softx.2015.06.001.
(52) Zhao, Y.; Truhlar, D. G. The M06 Suite of Density Functionals for Main Group Thermochemistry, Thermochemical Kinetics, Noncovalent Interactions, Excited States, and Transition Elements: Two New Functionals and Systematic Testing of Four M06-Class Functionals and 12 Other Functionals. *Theor. Chem. Acc.* **2008**, *120* (1), 215–241. https://doi.org/10.1007/s00214-007-0310-x.
(53) Cao, X.; Dolg, M. Segmented Contraction Scheme for Small-Core Lanthanide Pseudopotential Basis Sets. *J. Mol. Struct. THEOCHEM* **2002**, *581* (1), 139–147. https://doi.org/10.1016/S0166-1280(01)00751-5.
(54) Dolg, M.; Stoll, H.; Preuss, H. Energy-adjusted Ab Initio Pseudopotentials for the Rare Earth Elements. *J. Chem. Phys.* **1989**, *90* (3), 1730–1734. https://doi.org/10.1063/1.456066.
(55) Dunning, T. H., Jr. Gaussian Basis Sets for Use in Correlated Molecular Calculations. I. The Atoms Boron through Neon and Hydrogen. *J. Chem. Phys.* **1989**, *90* (2), 1007–1023. https://doi.org/10.1063/1.456153.

(56) Barone, V.; Cossi, M. Quantum Calculation of Molecular Energies and Energy Gradients in Solution by a Conductor Solvent Model. *J. Phys. Chem. A* **1998**, *102* (11), 1995–2001. https://doi.org/10.1021/jp9716997.
(57) O'Brien, R. D.; Summers, T. J.; Kaliakin, D. S.; Cantu, D. C. The Solution Structures and Relative Stability Constants of Lanthanide–EDTA Complexes Predicted from Computation. *Phys. Chem. Chem. Phys.* **2022**, *24* (17), 10263–10271. https://doi.org/10.1039/D2CP01081J.
(58) Douglas, M.; Kroll, N. M. Quantum Electrodynamical Corrections to the Fine Structure of Helium. *Ann. Phys.* **1974**, *82* (1), 89–155. https://doi.org/10.1016/0003-4916(74)90333-9.
(59) Hess, B. A. Applicability of the No-Pair Equation with Free-Particle Projection Operators to Atomic and Molecular Structure Calculations. *Phys. Rev. A* **1985**, *32* (2), 756–763. https://doi.org/10.1103/PhysRevA.32.756.
(60) Pantazis, D. A.; Chen, X.-Y.; Landis, C. R.; Neese, F. All-Electron Scalar Relativistic Basis Sets for Third-Row Transition Metal Atoms. *J. Chem. Theory Comput.* **2008**, *4* (6), 908–919. https://doi.org/10.1021/ct800047t.
(61) Zheng, J.; Xu, X.; Truhlar, D. G. Minimally Augmented Karlsruhe Basis Sets. *Theor. Chem. Acc.* **2011**, *128* (3), 295–305. https://doi.org/10.1007/s00214-010-0846-z.
(62) Dolg, J. *Computational Methods in Lanthanide and Actinide Chemistry;* Wiley. 2015.
(63) Neese, F. Software Update: The ORCA Program System—Version 5.0. *WIREs Comput. Mol. Sci.* **2022**, *12* (5), e1606. https://doi.org/10.1002/wcms.1606.
(64) Berendsen, H. J. C.; Postma, J. P. M.; van Gunsteren, W. F.; DiNola, A.; Haak, J. R. Molecular Dynamics with Coupling to an External Bath. *J. Chem. Phys.* **1984**, *81* (8), 3684–3690. https://doi.org/10.1063/1.448118.
(65) Perdew, J. P.; Burke, K.; Ernzerhof, M. Generalized Gradient Approximation Made Simple. *Phys. Rev. Lett.* **1996**, *77* (18), 3865–3868. https://doi.org/10.1103/PhysRevLett.77.3865.
(66) Kühne, T. D.; Iannuzzi, M.; Del Ben, M.; Rybkin, V. V.; Seewald, P.; Stein, F.; Laino, T.; Khaliullin, R. Z.; Schütt, O.; Schiffmann, F.; Golze, D.; Wilhelm, J.; Chulkov, S.; Bani-Hashemian, M. H.; Weber, V.; Borštnik, U.; Taillefumier, M.; Jakobovits, A. S.; Lazzaro, A.; Pabst, H.; Müller, T.; Schade, R.; Guidon, M.; Andermatt, S.; Holmberg, N.; Schenter, G. K.; Hehn, A.; Bussy, A.; Belleflamme, F.; Tabacchi, G.; Glöß, A.; Lass, M.; Bethune, I.; Mundy, C. J.; Plessl, C.; Watkins, M.; VandeVondele, J.; Krack, M.; Hutter, J. CP2K: An Electronic Structure and Molecular Dynamics Software Package - Quickstep: Efficient and Accurate Electronic Structure Calculations. *J. Chem. Phys.* **2020**, *152* (19), 194103. https://doi.org/10.1063/5.0007045.
(67) VandeVondele, J.; Krack, M.; Mohamed, F.; Parrinello, M.; Chassaing, T.; Hutter, J. Quickstep: Fast and Accurate Density Functional Calculations Using a Mixed Gaussian and Plane Waves Approach. *Comput. Phys. Commun.* **2005**, *167* (2), 103–128. https://doi.org/10.1016/j.cpc.2004.12.014.
(68) Goedecker, S.; Teter, M.; Hutter, J. Separable Dual-Space Gaussian Pseudopotentials. *Phys. Rev. B* **1996**, *54* (3), 1703–1710. https://doi.org/10.1103/PhysRevB.54.1703.
(69) VandeVondele, J.; Hutter, J. Gaussian Basis Sets for Accurate Calculations on Molecular Systems in Gas and Condensed Phases. *J. Chem. Phys.* **2007**, *127* (11), 114105. https://doi.org/10.1063/1.2770708.
(70) Lu, J.-B.; Cantu, D. C.; Nguyen, M.-T.; Li, J.; Glezakou, V.-A.; Rousseau, R. Norm-Conserving Pseudopotentials and Basis Sets To Explore Lanthanide Chemistry in Complex

Environments. *J. Chem. Theory Comput.* **2019**, *15* (11), 5987–5997. https://doi.org/10.1021/acs.jctc.9b00553.
(71) Grimme, S.; Antony, J.; Ehrlich, S.; Krieg, H; A consistent and accurate ab initio parametrization of density functional dispersion correction (DFT-D) for the 94 elements H-Pu. *J. Chem. Phys.* **2010,** 132 (15) https://doi.org/10.1063/1.3382344.
(72) Nosé, S. A Unified Formulation of the Constant Temperature Molecular Dynamics Methods. *J. Chem. Phys.* **1984**, *81* (1), 511–519. https://doi.org/10.1063/1.447334.
(73) Nosé, S. A Molecular Dynamics Method for Simulations in the Canonical Ensemble. *Mol. Phys.* **1984**, *52* (2), 255–268. https://doi.org/10.1080/00268978400101201.
(74) Palmer, B. J.; Pfund, D. M.; Fulton, J. L. Direct Modeling of EXAFS Spectra from Molecular Dynamics Simulations. *J. Phys. Chem.* **1996**, *100* (32), 13393–13398. https://doi.org/10.1021/jp960160q.
(75) Iwasawa, Y.; Asakura, K.; Tada, M. *XAFS Techniques for Catalysts, Nanomaterials, and Surfaces*. Springer Link, 2017.
(76) Ankudinov, A. L.; Ravel, B.; Rehr, J. J.; Conradson, S. D. Real-Space Multiple-Scattering Calculation and Interpretation of x-Ray-Absorption near-Edge Structure. *Phys. Rev. B* **1998**, *58* (12), 7565–7576. https://doi.org/10.1103/PhysRevB.58.7565.
(77) Rehr, J. J.; Kas, J. J.; Prange, M. P.; Sorini, A. P.; Takimoto, Y.; Vila, F. Ab Initio Theory and Calculations of X-Ray Spectra. *Comptes Rendus Phys.* **2009**, *10* (6), 548–559. https://doi.org/10.1016/j.crhy.2008.08.004.
(78) Rehr, J. J.; Albers, R. C. Theoretical Approaches to X-Ray Absorption Fine Structure. *Rev. Mod. Phys.* **2000**, *72* (3), 621–654. https://doi.org/10.1103/RevModPhys.72.621.
(79) Basset, J.; Denney, R. C.; Jeffery, G. H.; Mendham, J. *Vogel's Textbook of Quantitative Inorganic Analysis*, 4th ed.; Wiley, 1978.
(80) Ravel, B.; Newville, M. ATHENA, ARTEMIS, HEPHAESTUS: Data Analysis for X-Ray Absorption Spectroscopy Using IFEFFIT. *J. Synchrotron Radiat.* **2005**, *12* (4), 537–541. https://doi.org/10.1107/S0909049505012719.
(81) Bettencourt-Dias, A. de; Bauer, S.; Viswanathan, S.; Maull, B. C.; Ako, A. M. Unusual Nitro-Coordination of Europium(III) and Terbium(III) with Pyridinyl Ligands. *Dalton Trans.* **2012**, *41* (36), 11212–11218. https://doi.org/10.1039/C2DT31308A.
(82) Cotton, S. A.; Noy, O. E.; Liesener, F.; Raithby, P. R. Unequivocal Characterisation of a [Ln(Terpy)(NO3)3·(H2O)] Complex. *Inorganica Chim. Acta* **2003**, *344*, 37–42. https://doi.org/10.1016/S0020-1693(02)01266-5.
(83) Cotton, S. A.; Raithby, P. R. Systematics and Surprises in Lanthanide Coordination Chemistry. *Coord. Chem. Rev.* **2017**, *340*, 220–231. https://doi.org/10.1016/j.ccr.2017.01.011.
(84) Dutra, J. D. L.; Filho, M. A. M.; Rocha, G. B.; Freire, R. O.; Simas, A. M.; Stewart, J. J. P. Sparkle/PM7 Lanthanide Parameters for the Modeling of Complexes and Materials. *J. Chem. Theory Comput.* **2013**, *9* (8), 3333–3341. https://doi.org/10.1021/ct301012h.
(85) Bannwarth, C.; Ehlert, S.; Grimme, S. GFN2-xTB—An Accurate and Broadly Parametrized Self-Consistent Tight-Binding Quantum Chemical Method with Multipole Electrostatics and Density-Dependent Dispersion Contributions. *J. Chem. Theory Comput.* **2019**, *15* (3), 1652–1671. https://doi.org/10.1021/acs.jctc.8b01176.
(86) Bünzli, J.-C. G.; Milicic-Tang, A.; Mabillard, C. Lanthanide-Nitrate Interaction in Anhydrous Acetonitrile and Coordination Numbers of the Lanthanide Ions: FT–IR Study. *Helv. Chim. Acta* **1993**, *76* (3), 1292–1304. https://doi.org/10.1002/hlca.19930760316.

(87) Batatia, I.; Benner, P.; Chiang, Y.; Elena, A. M.; Kovács, D. P.; Riebesell, J.; Advincula, X. R.; Asta, M.; Avaylon, M.; Baldwin, W. J.; Berger, F.; Bernstein, N.; Bhowmik, A.; Blau, S. M.; Cărare, V.; Darby, J. P.; De, S.; Della Pia, F.; Deringer, V. L.; Elijošius, R.; El-Machachi, Z.; Falcioni, F.; Fako, E.; Ferrari, A. C.; Genreith-Schriever, A.; George, J.; Goodall, R. E. A.; Grey, C. P.; Grigorev, P.; Han, S.; Handley, W.; Heenen, H. H.; Hermansson, K.; Holm, C.; Jaafar, J.; Hofmann, S.; Jakob, K. S.; Jung, H.; Kapil, V.; Kaplan, A. D.; Karimitari, N.; Kermode, J. R.; Kroupa, N.; Kullgren, J.; Kuner, M. C.; Kuryla, D.; Liepuoniute, G.; Margraf, J. T.; Magdău, I.-B.; Michaelides, A.; Moore, J. H.; Naik, A. A.; Niblett, S. P.; Norwood, S. W.; O'Neill, N.; Ortner, C.; Persson, K. A.; Reuter, K.; Rosen, A. S.; Schaaf, L. L.; Schran, C.; Shi, B. X.; Sivonxay, E.; Stenczel, T. K.; Svahn, V.; Sutton, C.; Swinburne, T. D.; Tilly, J.; van der Oord, C.; Varga-Umbrich, E.; Vegge, T.; Vondrák, M.; Wang, Y.; Witt, W. C.; Zills, F.; Csányi, G. A Foundation Model for Atomistic Materials Chemistry. arXiv March 1, 2024. https://doi.org/10.48550/arXiv.2401.00096.

(88) Chen, C.; Ong, S. P. A Universal Graph Deep Learning Interatomic Potential for the Periodic Table. *Nat. Comput. Sci.* **2022**, *2* (11), 718–728. https://doi.org/10.1038/s43588-022-00349-3.

(89) Duvail, M.; Moreno Martinez, D.; Žiberna, L.; Guillam, E.; Dufrêche, J.-F.; Guilbaud, P. Modeling Lanthanide Ions in Solution: A Versatile Force Field in Aqueous and Organic Solvents. *J. Chem. Theory Comput.* **2024**, *20* (3), 1282–1292. https://doi.org/10.1021/acs.jctc.3c01162.

FOR TABLE OF CONTENTS ONLY